Preclinical Pharmacokinetics and Dosimetry Studies of ^{124}I/^{131}I-CLR1404 for Treatment of Pediatric Solid Tumors in Murine Xenograft Models

Ian R. Marsh[1], Joseph Grudzinski[1], Dana C. Baiu[2], Abigail Besemer[3], Reinier Hernandez[1], Justin J. Jeffery[4], Jamey P. Weichert[4], Mario Otto[2], and Bryan P. Bednarz[1]

[1]Department of Medical Physics, School of Medicine and Public Health, University of Wisconsin–Madison, Madison, Wisconsin; [2]Department of Pediatrics, Carbone Cancer Center, School of Medicine and Public Health, University of Wisconsin–Madison, Madison, Wisconsin; [3]Department of Radiation Oncology, University of Nebraska Medical Center, Omaha, Nebraska; and [4]Department of Radiology, School of Medicine and Public Health, University of Wisconsin–Madison, Madison, Wisconsin

Cancer is the second leading cause of death for children between the ages of 5 and 14 y. For children diagnosed with metastatic or recurrent solid tumors, for which the utility of external-beam radiotherapy is limited, the prognosis is particularly poor. The availability of tumor-targeting radiopharmaceuticals for molecular radiotherapy (MRT) has demonstrated improved outcomes in these patient populations, but options are nonexistent or limited for most pediatric solid tumors. 18-(*p*-iodophenyl)octadecylphosphocholine (CLR1404) is a novel antitumor alkyl phospholipid ether analog that broadly targets cancer cells. In this study, we evaluated the in vivo pharmacokinetics of ^{124}I-CLR1404 (CLR 124) and estimated theranostic dosimetry for ^{131}I-CLR1404 (CLR 131) MRT in murine xenograft models of the pediatric solid tumors neuroblastoma, rhabdomyosarcoma, and Ewing sarcoma. **Methods:** Tumor-bearing mice were imaged with small-animal PET/CT to evaluate the whole-body distribution of CLR 124 and, correcting for differences in radioactive decay, predict that of CLR 131. Image volumes representing CLR 131 provided input for Geant4 Monte Carlo simulations to calculate subject-specific tumor dosimetry for CLR 131 MRT. Pharmacokinetics for CLR 131 were extrapolated to adult and pediatric humans to estimate normal-tissue dosimetry. In neuroblastoma, a direct comparison of CLR 124 with ^{124}I-metaiodobenzylguanidine (^{124}I-MIBG) in an MIBG-avid model was performed. **Results:** In vivo pharmacokinetics of CLR 124 showed selective uptake and prolonged retention across all pediatric solid tumor models investigated. Subject-specific tumor dosimetry for CLR 131 MRT presents a correlative relationship with tumor-growth delay after CLR 131 MRT. Peak uptake of CLR 124 was, on average, 22% higher than that of ^{124}I-MIBG in an MIBG-avid neuroblastoma model. **Conclusion:** CLR1404 is a suitable theranostic scaffold for dosimetry and therapy with potentially broad applicability in pediatric oncology. Given the ongoing clinical trials for CLR 131 in adults, these data support the development of pediatric clinical trials and provide detailed dosimetry that may lead to improved MRT treatment planning.

Key Words: molecular radiotherapy; theranostic dosimetry; pediatric cancer; CLR1404; CLR 131

J Nucl Med 2019; 60:1414–1420
DOI: 10.2967/jnumed.118.225409

Cancer is the second leading cause of death in children 5–14 y old (*1*). Advances in treatment have increased the overall 5-y survival rate to approximately 80%, but improvements for several solid tumors have plateaued within the past 10–20 y (*2*). Most children diagnosed with primary disseminated or recurrent pediatric solid tumors such as neuroblastoma, rhabdomyosarcoma, or Ewing sarcoma have a particularly poor prognosis, despite the availability of highly toxic multimodality therapies (*3*).

External-beam radiotherapy plays an integral role in the treatment regimen for most pediatric solid tumors and has significantly contributed to improvements in overall survival over the decades. However, this mode of radiotherapy is limited to local control of primary tumor sites or larger masses (*4*). For patients with widespread metastatic disease, systemic tumor-targeting molecular radiotherapy (MRT) approaches are needed. The only well-studied and established radiotherapeutic agent in pediatric oncology is metaiodobenzylguanidine (MIBG), a norepinephrine analog for treatment of neuroblastoma (*5,6*). Since approximately 90% of all neuroblastoma cases will have MIBG-avid tumors, SPECT imaging with ^{123}I-MIBG is the recommended method of staging and evaluating response (*7,8*). As an MRT agent, ^{131}I-MIBG is used clinically as a monotherapy or in combination with chemotherapy and immunotherapy to treat neuroblastoma with curative or palliative intent. However, recent studies have shown that only 30% of patients who receive ^{131}I-MIBG MRT respond to treatment, and for those patients, the response is typically not curative (*9,10*). For other challenging pediatric solid tumors that are considered radiosensitive, such as rhabdomyosarcoma and Ewing sarcoma, there are no such MRT approaches available.

18-(*p*-iodophenyl)octadecylphosphocholine (known as NM404 or CLR1404) is an antitumor alkyl phospholipid ether analog that broadly targets cancer cells, with little uptake in normal tissue (*11*). Phospholipid ethers enter cells primarily via lipid rafts present at 6–10 times higher concentrations in plasma membranes of

Received Dec. 27, 2018; revision accepted Mar. 7, 2019.
For correspondence or reprints contact: Bryan P. Bednarz, Department of Medical Physics, 1005 WIMR, 1111 Highland Ave., Madison, WI 53705.
E-mail: bbednarz2@wisc.edu
Published online Mar. 29, 2019.

tumor cells than in normal cells (*11–14*). As an analog of naturally occurring phospholipids, CLR1404 is rapidly integrated into the membranes of cells and organelles. CLR1404 has the theranostic capacity to serve as a scaffold for delivery of ^{124}I (CLR 124) for PET imaging or ^{131}I (CLR 131) for MRT (*15*). We have confirmed uptake and tumoricidal effects in vitro and in vivo in more than 80 preclinical adult and pediatric cancer models (*15–19*). More significantly, tumor targeting has been confirmed in patients, and a variety of clinical trials for CLR 124 and CLR 131 are ongoing or have been completed (*20–22*).

In this work, we evaluate the tumor-selective uptake and biodistribution of CLR 124 in murine xenograft models of several pediatric solid tumors. In neuroblastoma, we perform a direct comparison to the clinical standard, MIBG. Normal-tissue dosimetry in adult and pediatric patients is estimated on the basis of extrapolated CLR 131 pharmacokinetics in human models. Subject-specific tumor dosimetry for CLR 131 MRT is calculated to demonstrate the theranostic utility of CLR 124 for MRT treatment planning in models with varying degrees of uptake.

MATERIALS AND METHODS

Radiopharmaceuticals

Clinical-grade CLR1404 and radiolabeled CLR 131 were kindly provided by Cellectar Biosciences. Methods for synthesis of CLR1404, radioiodination, and purification have been previously described (*11,15*). MIBG was obtained commercially (Sigma-Aldrich). ^{124}I-MIBG and CLR 124 were radiolabeled via isotope-exchange reaction (*23*) as previously reported (*18*). ^{124}I was obtained from IBA Molecular, and ^{131}I was obtained from Perkin Elmer. All radiopharmaceuticals were prepared under good-manufacturing-practice guidelines.

Pediatric Cancer Cells

Rh30 (alveolar rhabdomyosarcoma) and TC71 (Ewing sarcoma) were obtained from the Children's Oncology Group Cell Repository. The neuroblastoma lines CHLA20 and NB1691 were provided by Dr. Andrew Davidoff of St. Jude Children's Research Hospital. We have previously published on the tumor-selective uptake of CLR1404 in these cell lines in vitro (*16*). The lack of in vivo ^{124}I-MIBG uptake in conventional preclinical neuroblastoma models, despite good in vitro uptake, can be overcome with cell lines transduced with the human norepinephrine transporter (hNET) (*24,25*). The NB1691-hNET cell line used for comparison of CLR 124 and ^{124}I-MIBG was kindly provided by Dr. Katherine Matthay (University of California, San Francisco). All cell lines were cultured as described previously (*16,26*). The authenticity of cell lines obtained from noncommercial sources within 12 mo of the start of experiments is routinely verified via genomic short-tandem repeat profiling (University of Wisconsin–Madison Pathology Core Lab). Periodic polymerase chain reaction and HEK-Blue lipopolysaccharide testing (Invivogen) indicated that cells were free of bacterial contaminants, including *Mycoplasma* species.

Animal Models and Xenografts

All animal studies were conducted under National Institutes of Health guidelines and University of Wisconsin Institutional Animal Care and Use Committee–approved protocols. For in vivo experiments, NOD.Cg-Prkdc^{scid} Il2rg^{tm1Wjl}/SzJ (NSG) mice purchased from Jackson Laboratory were used. Groups of 4 mice were inoculated in subcutaneous tissue of the right flank with a 200-μL cell suspension containing 2×10^6 tumor cells to establish human tumor xenografts. Imaging studies commenced when tumor volumes reached approximately 150 mm^3, as described in a previous report on this investigation by Baiu et al. (*18*). After injection, the mice were housed individually in cages separated by lead shielding to minimize potential effects of cross irradiation.

PET/CT Imaging of CLR 124 and ^{124}I-MIBG

PET/CT studies investigating tumor uptake were conducted with Rh30, TC71, CHLA20, NB1691, and NB1691-hNET tumor–bearing NSG mice (4 each). Mice weighing 24.1 ± 2.5 g were administered 9.2 ± 0.7 MBq of CLR 124 or 9.7 ± 0.1 MBq of ^{124}I-MIBG via lateral tail vein injection for imaging. Under 2% isoflurane anesthesia in oxygen, the mice were imaged on an Inveon small-animal PET/CT scanner (Siemens). CLR 124 scans were acquired at 1–4, 24, 48, and 72 h after injection, with additional scans at 96, 120, 144, or 168 h. Mice administered ^{124}I-MIBG were scanned at 1, 4, 24, 48, and 72 h after injection to account for relatively faster biologic clearance observed in similar studies (*8,27*). During the uptake period before the first scan, the mice were kept conscious in room air.

PET scans were terminated after 40 million counts were collected in a 350- to 650-keV energy window and immediately followed by a CT scan without repositioning. The PET images were reconstructed using 3-dimensional ordered-subset expectation maximization followed by a maximum a posteriori algorithm into a 128 × 128 image matrix (0.78 × 0.78 × 0.80 mm resolution). Corrections for normalization, dead time, scatter, and attenuation were applied to the PET images as well as a ^{124}I-specific quantification calibration. The CT scans were acquired at an x-ray energy of 80 kVp at 1 mA for 275 ms with 220° of rotation and 220 backprojections. The resulting images were reconstructed via filtered backprojection using the Inveon Acquisition Workplace with a Shepp–Logan filter into a 480 × 480 image matrix (0.21 × 0.21 × 0.21 mm resolution). Data were analyzed by drawing regions of interest (ROIs) on the anatomic CT images. Image analysis was performed with AMIRA (FEI/Thermo Fisher Scientific).

Calculation of percentage injected dose per gram (%ID/g) assumed a tissue density of water for all ROIs except lung, for which 0.5 g/cm^3 was used. For the direct comparison of CLR 124 and ^{124}I-MIBG, regions encompassing tumor and contralateral muscle volumes were analyzed. The residence time of CLR 131 and ^{131}I-MIBG in tumor and muscle was calculated after decay correction of the biodistributions. The residence time tumor-to-muscle ratio was used to quantitatively compare the tumor selectivity of the agents.

Radiation Dosimetry Extrapolation to Humans

Dosimetry for normal tissues was performed using OLINDA/EXM (version 1.1) (*28*). Estimated absorbed dose delivered to organs in humans was based on the mean %ID/g of CLR 124 observed in PET/CT scans of mice. Pharmacokinetics were decay-corrected to represent CLR 131 and extrapolated (*29*) to 5-y-old pediatric and adult human standardized phantoms:

$$\left(\frac{\%\text{ID}}{m_{\text{organ}}}\right)_{\text{human}} = \left(\frac{\%\text{ID}}{m_{\text{organ}}}\right)_{\text{animal}} \times \left[\frac{\left(m_{\text{whole body}}\right)_{\text{animal}}}{\left(m_{\text{whole body}}\right)_{\text{human}}}\right] \qquad \text{Eq. 1}$$

where m is the mass of the region. The biodistribution of CLR 124 in humans is thus assumed in Equation 1 to be the same as that observed in animal models. The time–activity curve was modeled with a trapezoidal fit from the time of injection through each PET/CT scan and followed by exponential radioactive decay from the final time point. Effective doses output from OLINDA are calculated using weighting factors from International Commission on Radiological Protection Publication 103 (*30*).

Three-Dimensional CLR 131 Dosimetry

The OLINDA/EXM approach to tumor dosimetry with isolated unit-density spheres and uniform activity distributions lacks the context of surrounding normal tissue with nonnegligible uptake and can

lead to unrepresentative dosimetry. Voxel-based dosimetry allows for analysis of heterogeneous distributions, which can lead to clinically relevant radiobiologic implications. To achieve more subject-specific tumor dosimetry, we used the RAPID (Radiopharmaceutical Assessment Platform for Internal Dosimetry) workflow as we have previously described in detail (*31,32*).

Absorbed dose rate distributions at each time point were generated from Geant4 (version 9.6) Monte Carlo simulations using CT and PET volumes to define geometry and source distributions, respectively. Over 10,000 decays of ^{131}I were sampled uniformly in each source voxel, or approximately 4.7×10^8 decays per subject, to achieve less than a 1% relative error in each ROI. The absorbed dose rate within ROIs was then averaged, and the integral absorbed dose to the tumor was calculated. The time–dose-rate curve was similarly modeled with a trapezoidal exponential fit. The prolonged retention of CLR 131 assumed in the final extrapolation is supported by observations from previous clinical studies (*21*).

The dose–response relationship for CLR 131 is evaluated through the context of tumor growth delay from efficacy studies we have previously published as part of this investigation (*18*). In these efficacy studies, mice bearing Rh30, TC71, CHLA20, and NB1691 flank tumor xenografts (6–9 each) were administered a single fraction of CLR 131, which significantly slowed growth in all tumor models relative to control mice treated with an equivalent mass of nonradioactive CLR1404. Tumor doubling time (TDT) was estimated from the slope of semilogarithmic plots of tumor volume against time (*33*). Specific growth delay (SGD) was defined as the number of tumor volume doublings delayed by the treatment:

$$\mathrm{SGD} = \frac{\mathrm{TDT}_{\mathrm{CLR\,131}} - \mathrm{TDT}_{\mathrm{control}}}{\mathrm{TDT}_{\mathrm{control}}}. \qquad \text{Eq. 2}$$

Statistical Analysis

Quantitative values are expressed as mean ± SD, with all error bars denoting SE or the mean, unless otherwise stated.

RESULTS

Radiolabeling

Isolated radiochemical yields for CLR 131 were consistently above 70%, as determined by high-performance liquid chromatography. Specific activity of CLR 131 ranged between 0.74 and 2.59×10^9 MBq/mol (mean, 1.85×10^9 MBq/mol), with radiochemical purity over 96% in all cases.

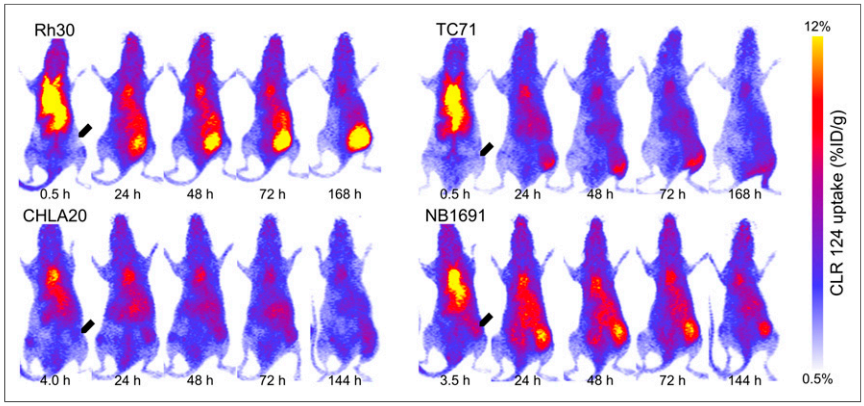

FIGURE 1. PET/CT imaging of NSG mice with established pediatric solid tumor xenografts (arrows) after intravenous injection of 9.2 ± 0.7 MBq of CLR 124. Maximum-intensity projections of representative mice in each cohort are shown at 5 time points after injection.

PET/CT Imaging and In Vivo Biodistribution of CLR 124

Longitudinal PET/CT imaging studies were performed over 144–168 h for groups of mice (4 each) bearing Rh30, TC71, CHLA20, and NB1691 xenografts. One animal in the NB1691 cohort died partway through the imaging study and is excluded from these results. Maximum-intensity projections at each time point are shown to illustrate temporal changes in biodistribution of CLR 124 for representative mice in each cohort (Fig. 1). ROIs were contoured, and the fused PET/CT images were used to quantify the CLR 124 biodistribution (Fig. 2). The heart, representative of blood pool, showed the highest concentration at 1.5 h after injection (15.89 ± 3.69 %ID/g, $n = 15$), decreasing thereafter through a rapid initial distribution phase followed by a prolonged terminal phase. The pharmacokinetics of the lung displayed markedly similar clearance due to high perfusion through the volume. Accumulation in the liver and kidneys was initially measured at 9.63 ± 1.54 and 7.36 ± 0.87 %ID/g, respectively ($n = 15$). After 168 h, accumulation of CLR 124 decreased by 65% in the liver and by 57% the kidneys. Uptake in the brain and bone marrow was minimal, with little clearance observed from the initial values of 1.89 ± 0.33 and 3.30 ± 0.54 %ID/g, respectively. Differences between the normal-tissue pharmacokinetics of the xenograft models were negligible.

Tumor-selective uptake and prolonged retention of CLR 124 was observed in all tumor models investigated (Fig. 3). CHLA20 and NB1691 tumors exhibited peak uptake of 4.51 ± 1.30 ($n = 4$) and 5.85 ± 1.07 %ID/g ($n = 4$), respectively, at 144 h, whereas Rh30 and TC71 tumors achieved concentrations of 7.44 ± 1.78 ($n = 4$) and 4.72 ± 1.12 %ID/g ($n = 3$), respectively, at 48–72 h after injection.

CLR 131 Dosimetry

Radiation dosimetry for single-fraction CLR 131 MRT was estimated using the biodistribution of CLR 124 in tumor-bearing NSG mouse models (Fig. 2). Estimates of absorbed dose corresponding to human organs are summarized in Table 1. For pediatric patients, calculations showed high doses to heart wall (2.67 ± 0.28 mSv/MBq), liver (2.52 ± 0.38 mSv/MBq), osteogenic cells (2.51 ± 0.20 mSv/MBq), and kidneys (2.28 ± 0.32 mSv/MBq). In adult patients, these same organs received the highest dose, with estimated values 66%–70% less than in children, as expected. Absorbed dose to bone marrow was estimated at 1.83 ± 0.15 for pediatric and 0.50 ± 0.04 mSv/MBq for adult patients, a particularly important observation as this has been the dose-limiting factor for CLR 131 MRT.

Estimated integral absorbed dose prescriptions and the requisite administered activity to achieve therapeutic doses of 20 Gy to tumors in Rh30, TC71, CHLA20, and NB1691 cohorts is shown in Table 2. Consistent with tumor-selective uptake, Rh30 tumors received the highest integral absorbed dose after 3 half-lives, at 1.81 ± 0.43 Gy/MBq, followed by NB1691 (1.10 ± 0.16 Gy/MBq), TC71 (0.94 ± 0.16 Gy/MBq), and CHLA20 (0.81 ± 0.32 Gy/MBq). Initial tumor volumes ranged between 48 and 615 mm^3 (mean, 324 ± 180 mm^3).

To assess the radiotherapeutic properties of CLR 131 in pediatric solid tumors, groups of 6–9 NSG mice bearing Rh30,

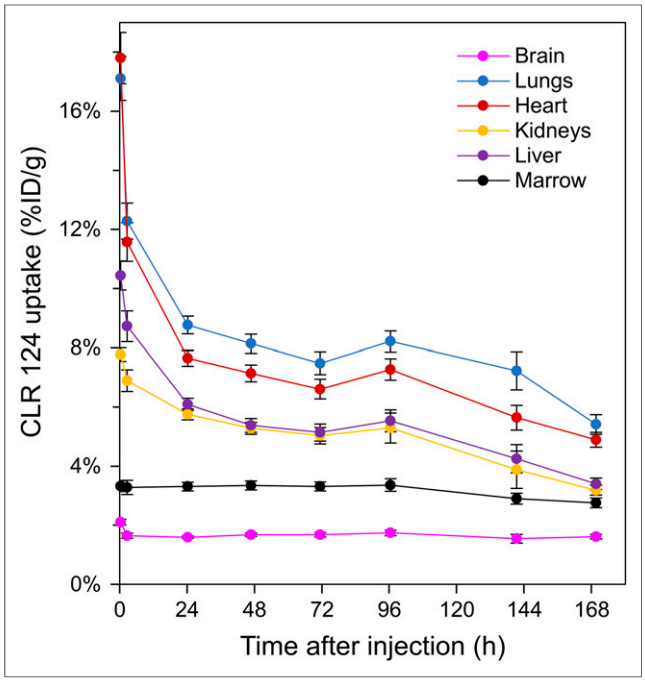

FIGURE 2. Pharmacokinetic profiles of CLR 124 uptake in liver, kidneys, lungs, heart, brain, and bone marrow after intravenous injection. Mean uptake is shown at each time point (n = 15) with error bars for SE.

TC71, CHLA20, and NB1691 xenografts were administered either 3.15–3.81 MBq of CLR 131 (mean, 3.40 ± 0.20 MBq) or an equivalent mass of nonradioactive CLR1404. Tumor growth and survival were assessed through 50 d after injection while the mice were monitored for radiotoxicity. An earlier report on this

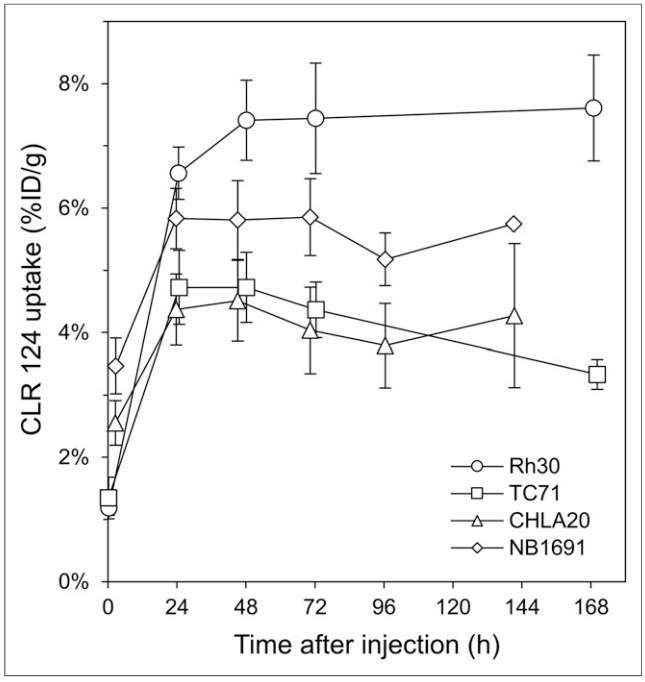

FIGURE 3. Tumor uptake in murine xenograft models of Rh30, TC71, CHLA20 (n = 4), and NB1691 (n = 3) is shown as mean %ID/g with error bars for SE.

TABLE 1
Estimated Absorbed Radiation Doses to Organs from Intravenous Administration of CLR 131 in Pediatric and Adult Humans

Organ	Child (n = 14; mSv/MBq)	Adult (n = 14; mSv/MBq)
Adrenals	1.425 ± 0.125	0.446 ± 0.041
Brain	0.969 ± 0.058	0.278 ± 0.017
Breasts	1.103 ± 0.094	0.335 ± 0.029
Gallbladder wall	1.444 ± 0.131	0.471 ± 0.045
Lower large intestine wall	1.346 ± 0.111	0.426 ± 0.036
Small intestine	1.420 ± 0.119	0.438 ± 0.038
Stomach wall	1.346 ± 0.115	0.420 ± 0.037
Upper large intestine wall	1.409 ± 0.119	0.434 ± 0.038
Heart wall	2.673 ± 0.283	0.790 ± 0.085
Kidneys	2.278 ± 0.320	0.669 ± 0.092
Liver	2.516 ± 0.384	0.750 ± 0.114
Lungs	1.888 ± 0.238	0.559 ± 0.070
Muscle	1.219 ± 0.101	0.373 ± 0.032
Ovaries	1.404 ± 0.117	0.438 ± 0.037
Pancreas	1.471 ± 0.130	0.457 ± 0.041
Red marrow	1.825 ± 0.145	0.496 ± 0.041
Osteogenic cells	2.506 ± 0.199	0.840 ± 0.070
Skin	1.053 ± 0.088	0.314 ± 0.027
Spleen	1.346 ± 0.115	0.410 ± 0.036
Testes	1.184 ± 0.098	0.367 ± 0.031
Thymus	1.294 ± 0.108	0.404 ± 0.036
Thyroid	1.326 ± 0.109	0.384 ± 0.033
Urinary bladder wall	1.330 ± 0.110	0.420 ± 0.036
Uterus	1.417 ± 0.118	0.441 ± 0.038
Total body	1.376 ± 0.119	0.406 ± 0.036

Organ dosimetry shows absorbed radiation doses based on CLR 124 uptake data from 14 tumor-bearing mice extrapolated to 5-y-old and adult human models.

investigation by Baiu et al. (*18*) showed significantly reduced tumor growth in all pediatric solid tumor models during the initial 21–28 d after injection. Here, tumor growth response to CLR 131 was evaluated against the estimated integral absorbed dose delivered after 3 half-lives (24 d) (Fig. 4). As expected, the Rh30 cohort that received the highest absorbed dose (5.83 ± 1.19 Gy) also exhibited the largest specific growth delay response. However, despite receiving the second highest dose, the NB1691 cohort displayed a smaller specific growth delay response than either the CHLA20 or the TC71 group. Varying levels of response to the same injected activity of CLR 131 observed in these data emphasizes the importance of personalized dosimetry in MRT.

CLR 124 and ^{124}I-MIBG in Murine hNET-NB1691 Xenografts

Longitudinal PET/CT imaging studies were performed over 72 or 120 h for mice bearing hNET-NB1691 xenografts administered either ^{124}I-MIBG or CLR 124, respectively. Representative 3-dimensional renderings of PET/CT volumes for each cohort are

TABLE 2
Subject-Specific Tumor Dosimetry in Murine Xenograft Models of Rh30, TC71, CHLA20, and NB1691 for CLR 131 MRT

Xenograft	Integral prescription dose (Gy/MBq)			CLR 131 (MBq) to deliver 20 Gy
	8 d	24 d	∞	
Rh30	0.98 ± 0.19	1.81 ± 0.37	2.08 ± 0.43	9.59 ± 1.98
TC71	0.57 ± 0.11	0.94 ± 0.16	1.06 ± 0.18	18.92 ± 3.18
CHLA20	0.47 ± 0.16	0.81 ± 0.32	0.92 ± 0.37	21.68 ± 8.72
NB1691	0.64 ± 0.10	1.10 ± 0.16	1.26 ± 0.18	15.92 ± 2.29

Integral prescription dose to tumor is shown calculated out to 1 and 3 times half-life of ^{131}I, as well as committed dose integrated out to infinity.

shown at time points representing peak tumor-specific uptake (Fig. 5A). Accumulation of CLR 124 was highest at 44 h (2.86 ± 0.49 %ID/g, $n = 4$), and although ^{124}I-MIBG achieved peak uptake at 4 h (2.35 ± 1.46 %ID/g, $n = 4$), measured values were not statistically significantly different from muscle until 24 h after injection (0.63 ± 0.15 %ID/g) (Fig. 5B). The residence time tumor-to-muscle ratios of CLR 131 and ^{131}I-MIBG were determined to be 2.5 ± 0.6 and 1.9 ± 0.6, respectively. This measure of tumor-specific uptake was similar for both agents, suggesting a potentially similar therapeutic efficacy in this model.

DISCUSSION

We have characterized the pharmacokinetics and performed dosimetry for the theranostic tumor-targeted MRT agent CLR1404 in murine xenograft models of neuroblastoma, rhabdomyosarcoma, and Ewing sarcoma. PET/CT imaging of CLR 124 in vivo supports the suggestion of selective uptake and prolonged retention of CLR1404 in pediatric solid tumors shown in previous in vitro investigations (*16*). This is further corroborated by significant in vivo antitumor efficacy after CLR 131 MRT in murine xenograft models of the same cell lines (*18*). Absorbed doses to normal tissues in pediatric and adult humans from single-fraction CLR 131 MRT were estimated via extrapolated preclinical CLR 124 imaging. We report here a direct comparison of tumor-selective uptake of CLR1404 against the clinically available MIBG in murine xenograft models of neuroblastoma that suggests similar efficacy of the 2 MRT agents. Given the clinically beneficial effects of MIBG therapy for neuroblastoma, radiolabeled CLR1404 could have a profound impact for patients with rhabdomyosarcoma, Ewing sarcoma, neuroblastoma, and potentially other pediatric solid tumors. Detailed investigations of the pharmacokinetic and dosimetric behavior of CLR1404 in preclinical models, as presented herein, are essential for successful clinical translation.

To evaluate the potential efficacy of CLR 131 MRT in pediatric neuroblastoma, the agent must ultimately be compared with ^{131}I-MIBG, the current standard of care. We have presented here a direct comparison of the tumor-selective uptake of CLR 124 and ^{124}I-MIBG in the NB1691-hNET model (Fig. 5). NB1691-hNET has been established as a reliable in vivo model for ^{124}I-MIBG uptake in neuroblastoma (*27*). Although the mechanism for uptake and biologic clearance is fundamentally different, the calculated residence time of CLR 131 and ^{131}I-MIBG in tumor and contralateral muscle provides an apt comparison. The residence-time tumor-to-muscle ratio was 2.5 ± 0.6 for CLR 131 and 1.9 ± 0.6 for ^{131}I-MIBG (4 each), indicating similar tumor specificity toward neuroblastoma. This suggests that CLR 131 could potentially deliver similar therapeutic efficacy to what has been established for ^{131}I-MIBG. The prolonged retention of CLR1404 allows for a relatively higher dose per injected activity and thus smaller requisite activity for MRT. Since a thyroid blockade was not implemented before administration, the stability of the radiotracers in vivo may have affected the results. Elevated uptake near the thyroid in ^{124}I-MIBG mice is qualitatively observed in Figure 5 but is absent in CLR 124 mice. This finding is particularly significant given the rapid clearance of ^{124}I-MIBG (24–48 h) compared with CLR 124 (over 120 h) and may suggest that ^{124}I-MIBG is less radiochemically

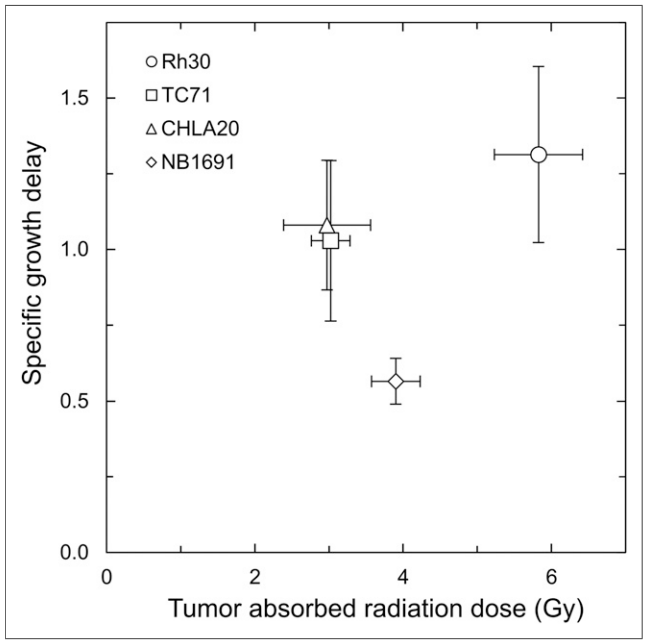

FIGURE 4. Dose–response relations for mice with Rh30, TC71, CHLA20, and NB1691 xenografts and treated with single dose of CLR 131 MRT. Integral absorbed doses (*x*-axis) were calculated after 3 half-lives (24 d) after injection for each subject. Tumor growth response is expressed on vertical axis as mean specific growth delay for Rh30, TC71, CHLA20, and NB1691 ($n = 7$, 7, 6, and 9, respectively) with error bars for SE.

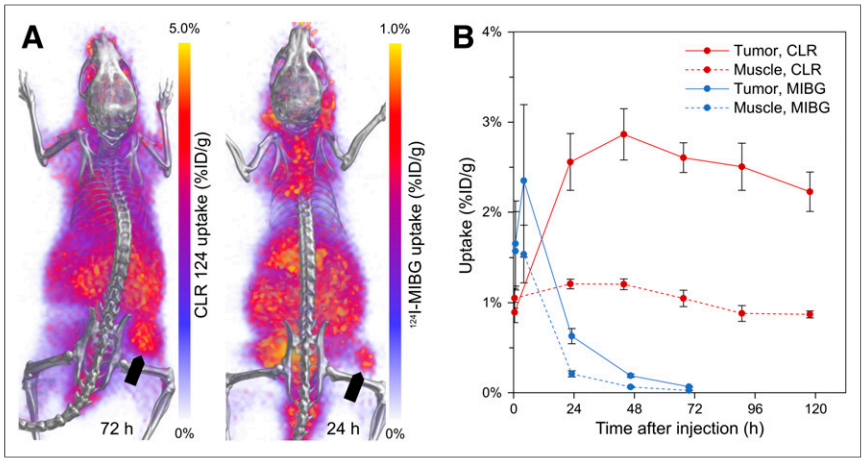

FIGURE 5. Whole-body PET/CT imaging and quantitative analysis of tumor-specific uptake of CLR 124 and ^{124}I-MIBG in murine xenograft models of NB1691-hNET. (A) Representative murine xenograft models of NB1691-hNET administered CLR 124 or ^{124}I-MIBG are presented as 3-dimensional renderings of PET (purple and yellow) fused with CT (grayscale) images acquired during peak tumor-specific uptake at 72 and 24 h after injection, respectively. Location of flank tumor is indicated by arrows. (B) PET/CT ROI analysis of tumor and contralateral muscle uptake is shown with mean values (n = 4) and error bars for SE.

stable in vivo relative to CLR 124. However, Friedman et al. showed that physiologic uptake of MIBG in the thyroid gland, attributable to the many sympathetic nerve endings therein, is expected despite the use of a thyroid blockade (*34*). Given that thyroid blocking is typically used for clinical radioiodine MRT, its absence is a limitation of this direct comparison.

A notable limitation of this work is the uncertainty inherent in the method of extrapolating preclinical pharmacokinetics to human models (*35*). This uncertainty then extends to the estimated CLR 131 normal-tissue dosimetry we have presented for pediatric and adult humans. The context through which to evaluate the accuracy of this dosimetry can be found in previously published work evaluating the dosimetry of CLR 131 for adult patients with relapsed or refractory solid tumors (*20,22*). Absorbed dose to the liver was estimated at 1.09 ± 0.33 mSv/MBq by Grudzinski et al. with SPECT/planar-based dosimetry and 0.87 ± 0.29 mSv/MBq by Lubner et al. with SPECT/CT-based dosimetry, 45% and 16% higher, respectively, than our estimate of 0.75 ± 0.11 mSv/MBq (Table 1). However, the 0.56 ± 0.03 and 0.55 ± 0.08 mSv/MBq reportedly delivered to the dose-limiting red marrow were only 14% and 10% higher, respectively, than our estimate of 0.50 ± 0.04 mSv/MBq. The conservative assumption of purely radioactive decay after the final imaging time point (168 h) in our work neglects the contribution of biologic clearance observed in normal tissues (Fig. 2). Imaging studies in these clinical trials were performed through 336–504 h after injection and may have better accounted for biologic clearance. This clearance is more significant in the liver than in the marrow, which may contribute to the differences in comparisons between the studies. The high percentage of tumor burden per body weight in our mouse models (1.36%), combined with significant tumor uptake, could account for the smaller estimated absorbed doses to normal tissues. Although CLR 131 SPECT and extrapolated preclinical theranostic CLR 131 dosimetry are by no means a direct comparison, the similarity of these normal-tissue dosimetry estimates supports the suggested theranostic ability of CLR 124 to serve as a pretherapy biomarker for CLR 131 MRT. The higher estimates for normal-tissue dosimetry in pediatric relative to adult models has also been observed in similar studies (*36*) and suggests using a lower starting dose in a phase I pediatric clinical trial. Higher dose delivered to red marrow could potentially be accounted for with autologous hematopoietic stem cell support to avoid prolonged myelosuppression toxicity. However, pretherapy theranostic dosimetry via CLR 124 PET/CT imaging would provide a more accurate and personalized starting dose.

The range in requisite activity to deliver therapeutic doses to tumor volumes in our models (Table 2) indicate variable efficacy in the cell lines investigated. On the basis of dosimetry alone, CLR 131 MRT treatments for rhabdomyosarcoma (Rh30) and neuroblastoma (NB1691) appear most promising. However, in evaluating dose response, we showed that identical administrations of CLR 131 can achieve similar efficacy in Ewing sarcoma and neuroblastoma (Fig. 4). In the clinic, these discrepancies may be minimized with pretherapy CLR 124 PET/CT for screening and more personalized CLR 131 MRT treatment planning. Even with highly restrictive screening, the potential for CLR1404 to provide a currently nonexistent MRT treatment option for patients with cancers such as Ewing sarcoma would have a significant impact in pediatric oncology.

CONCLUSION

Herein, we present preclinical pharmacokinetics and tumor dosimetry for theranostic CLR 124 and CLR 131 suggesting tumor-specific uptake in murine xenograft models of neuroblastoma, rhabdomyosarcoma, and Ewing sarcoma. A direct comparison of CLR1404 to the standard of care, MIBG, in an established preclinical model of MIBG-avid neuroblastoma is shown with similar tumor selectivity. The internal dosimetry estimates of absorbed dose received by normal tissues in pediatric and adult human models provide a valuable reference for a pediatric clinical trial that is in development at this institution. Furthermore, the method of subject-specific 3-dimensional tumor dosimetry is presented to demonstrate its applicability to theranostic treatment planning of CLR 131 MRT.

DISCLOSURE

Jamey Weichert was a cofounder of Cellectar Biosciences. This work was supported by NIH R21CA198392-01, the Midwest Athletes Against Childhood Cancer Foundation, Hyundai Hope on Wheels, SU2C/St. Baldrick's Pediatric Dream Team Translational Research Grant SU2C-AACR-DT1113, and NIH/NCI P30 CA014520. No other potential conflict of interest relevant to this article was reported.

ACKNOWLEDGMENT

We thank University of Wisconsin–Madison Small Animal Imaging and Radiotherapy Facility of the University of Wisconsin Carbone Cancer Center for its support.

KEY POINTS

QUESTION: How well does CLR1404 target pediatric solid tumors in vivo, and what level of absorbed dose is expected in tumors and normal tissues in humans?

PERTINENT FINDINGS: We characterized the in vivo pharmacokinetics of CLR 124 and confirmed tumor-selective uptake in preclinical mouse models of the pediatric solid tumors neuroblastoma, rhabdomyosarcoma, and Ewing sarcoma. Theranostic subject-specific tumor dosimetry was performed for CLR 131 MRT, and estimates of absorbed dose to normal tissues in pediatric and adult humans are provided.

IMPLICATIONS FOR PATIENT CARE: CLR 131 MRT with pretherapy CLR 124 could have a profound impact on patients with rhabdomyosarcoma, Ewing sarcoma, neuroblastoma, and potentially other pediatric solid tumors.

REFERENCES

1. Ward E, DeSantis C, Robbins A, Kohler B, Jemal A. Childhood and adolescent cancer statistics, 2014. *CA Cancer J Clin.* 2014;64:83–103.
2. Smith MA, Seibel NL, Altekruse SF, et al. Outcomes for children and adolescents with cancer: challenges for the twenty-first century. *J Clin Oncol.* 2010;28: 2625–2634.
3. Chen X, Pappo A, Dyer MA. Pediatric solid tumor genomics and developmental pliancy. *Oncogene.* 2015;34:5207–5215.
4. Park JR, Bagatell R, London WB, et al. Children's Oncology Group's 2013 blueprint for research: neuroblastoma. *Pediatr Blood Cancer.* 2013;60:985–993.
5. Short JH, Darby TD. Sympathetic nervous system blocking agents. III. Derivatives of benzylguanidine 1-3. *J Med Chem.* 1967;10:833–840.
6. Wieland DM, Brown LE, Tobes MC, et al. Imaging the primate adrenal medulla with [^{123}I] and [^{131}I] meta-iodobenzylguanidine: concise communication. *J Nucl Med.* 1981;22:358–364.
7. Taggart D, Dubois S, Matthay KK. Radiolabeled metaiodobenzylguanidine for imaging and therapy of neuroblastoma. *Q J Nucl Med Mol Imaging.* 2008;52:403–418.
8. Matthay KK, Shulkin B, Ladenstein R, et al. Criteria for evaluation of disease extent by ^{123}I-metaiodobenzylguanidine scans in neuroblastoma: a report for the International Neuroblastoma Risk Group (INRG) Task Force. *Br J Cancer.* 2010; 102:1319–1326.
9. Wilson JS, Gains JE, Moroz V, Wheatley K, Gaze MN. A systematic review of ^{131}I-meta iodobenzylguanidine molecular radiotherapy for neuroblastoma. *Eur J Cancer.* 2014;50:801–815.
10. Sung KW. Treatment of high-risk neuroblastoma. *Korean J Pediatr.* 2012;55: 115–120.
11. Pinchuk AN, Rampy MA, Longino MA, et al. Synthesis and structure-activity relationship effects on the tumor avidity of radioiodinated phospholipid ether analogues. *J Med Chem.* 2006;49:2155–2165.
12. Carrasco MP, Jiménez-López JM, Ríos-Marco P, Segovia JL, Marco C. Disruption of cellular cholesterol transport and homeostasis as a novel mechanism of action of membrane-targeted alkylphospholipid analogues. *Br J Pharmacol.* 2010;160:355–366.
13. Li YC, Park MJ, Ye S-K, Kim C-W, Kim Y-N. Elevated levels of cholesterol-rich lipid rafts in cancer cells are correlated with apoptosis sensitivity induced by cholesterol-depleting agents. *Am J Pathol.* 2006;168:1107–1118.
14. Patra SK. Dissecting lipid raft facilitated cell signaling pathways in cancer. *Biochim Biophys Acta.* 2008;1785:182–206.
15. Weichert JP, Clark PA, Kandela IK, et al. Alkylphosphocholine analogs for broad-spectrum cancer imaging and therapy. *Sci Transl Med.* 2014;6:240ra75.
16. Marino R, Baiu DC, Bhattacharya S, et al. Tumor-selective anti-cancer effects of the synthetic alkyl phosphocholine analog CLR1404 in neuroblastoma. *Am J Cancer Res.* 2015;5:3422–3435.
17. Grudzinski J, Marsh I, Titz B, et al. CLR 125 Auger electrons for the targeted radiotherapy of triple-negative breast cancer. *Cancer Biother Radiopharm.* 2018; 33:87–95.
18. Baiu DC, Marsh IR, Boruch AE, et al. Targeted molecular radiotherapy of pediatric solid tumors using a radioiodinated alkyl-phospholipid ether analog. *J Nucl Med.* 2018;59:244–250.
19. Morris ZS, Weichert JP, Saker J, et al. Therapeutic combination of radiolabeled CLR1404 with external beam radiation in head and neck cancer model systems. *Radiother Oncol.* 2015;116:504–509.
20. Grudzinski JJ, Titz B, Kozak K, et al. A phase 1 study of ^{131}I-CLR1404 in patients with relapsed or refractory advanced solid tumors: dosimetry, biodistribution, pharmacokinetics, and safety. *PLoS One.* 2014;9:e111652.
21. Deming DA, Maher ME, Leystra AA, et al. Phospholipid ether analogs for the detection of colorectal tumors. *PLoS One.* 2014;9:e109668.
22. Lubner SJ, Mullvain J, Perlman S, et al. A phase 1, multi-center, open-label, dose-escalation study of ^{131}I-CLR1404 in subjects with relapsed or refractory advanced solid malignancies. *Cancer Invest.* 2015;33:483–489.
23. Mangner TJ, Wu JL, Wieland DM. Solid-phase exchange radioiodination of aryl iodides: facilitation by ammonium sulfate. *J Org Chem.* 1982;47:1484–1488.
24. McCluskey AG, Boyd M, Ross SC, et al. [^{131}I]meta-iodobenzylguanidine and topotecan combination treatment of tumors expressing the noradrenaline transporter. *Clin Cancer Res.* 2005;11:7929–7937.
25. Moroz MA, Serganova I, Zanzonico P, et al. Imaging hNET reporter gene expression with ^{124}I-MIBG. *J Nucl Med.* 2007;48:827–836.
26. Kang MH, Smith MA, Morton CL, Keshelava N, Houghton PJ, Reynolds CP. National Cancer Institute pediatric preclinical testing program: model description for in vitro cytotoxicity testing. *Pediatr Blood Cancer.* 2011;56:239–249.
27. Seo Y, Gustafson WC, Dannoon SF, et al. Tumor dosimetry using [^{124}I]miodobenzylguanidine microPET/CT for [^{131}I]m-iodobenzylguanidine treatment of neuroblastoma in a murine xenograft model. *Mol Imaging Biol.* 2012;14:735–742.
28. Stabin MG, Sparks RB, Crowe E. OLINDA/EXM: the second-generation personal computer software for internal dose assessment in nuclear medicine. *J Nucl Med.* 2005;46:1023–1027.
29. Waxler SH, Enger M. Organ weights and obesity in mice. *J Nutr.* 1954;54: 209–214.
30. ICRP. The 2007 recommendations of the international commission on radiological protection: ICRP publication 103. *Ann ICRP.* 2007;37:1–332.
31. Besemer AE, Yang YM, Grudzinski JJ, Hall LT, Bednarz BP. Development and validation of RAPID: a patient-specific Monte Carlo three-dimensional internal dosimetry platform. *Cancer Biother Radiopharm.* 2018;33:155–165.
32. Besemer AE, Grudzinski JJ, Weichert JP, Hall LT, Bednarz BP. Pretreatment CLR 124 positron emission tomography accurately predicts CLR 131 three-dimensional dosimetry in triple-negative breast cancer patient. *Cancer Biother Radiopharm.* 2019;34:13–23.
33. Rutgers M, Buitenhuis CKM, Hoefnagel CA, Voûte PA, Smets LA. Targeting of meta-iodobenzylguanidine to SK-N-SH human neuroblastoma xenografts: tissue distribution, metabolism and therapeutic efficacy. *Int J Cancer.* 2000;87:412–422.
34. Friedman NC, Hassan A, Grady E, Matsuoka DT, Jacobson AF. Efficacy of thyroid blockade on thyroid radioiodine uptake in ^{123}I-mIBG imaging. *J Nucl Med.* 2014;55:211–215.
35. Luoto P, Laitinen I, Suilamo S, Någren K, Roivainen A. Human dosimetry of carbon-11 labeled N-butan-2-yl-1-(2-chlorophenyl)-N-methylisoquinoline-3-carboxamide extrapolated from whole-body distribution kinetics and radiometabolism in rats. *Mol Imaging Biol.* 2010;12:435–442.
36. Lee CL, Wahnishe H, Sayre GA, et al. Radiation dose estimation using preclinical imaging with ^{124}I-metaiodobenzylguanidine (MIBG) PET. *Med Phys.* 2010;37:4861–4867.